NANO MICRO small

# Supporting Information

for *Small,* DOI: 10.1002/smll.202101100

## In Situ Observation of Low-Power Nano-Synaptic Response in Graphene Oxide Using Conductive Atomic Force Microscopy

*Fei Hui,* Peisong Liu, Stephen A. Hodge, Tian Carey, Chao Wen, Felice Torrisi, D. Thanuja L. Galhena, Flavia Tomarchio, Yue Lin, Enrique Moreno, Juan B. Roldan, Elad Koren, Andrea C. Ferrari, and Mario Lanza**

# Supporting Information

## Low-Power Nano-Synaptic Response in Graphene Oxide

*Fei Hui*, Peisong Liu, Stephen A. Hodge, Tian Carey, Chao Wen, Felice Torrisi, D. Thanuja L. Galhena, Flavia Tomarchio, Yue Lin, Enrique Moreno, Juan B. Roldan, Elad Koren, Andrea C. Ferrari, Mario Lanza**

**Table S1**. Summary of typical synaptic behaviors of artificial synaptic electronic devices. SLG: Single layer graphene; SM = sensory memory; LTM = long term memory; STP = short term plasticity; LTP = long term plasticity; LTD = long term depression; STDP = spike-timing dependent plasticity; SRDP = spike response dependent plasticity; PPF = paired-pulse facilitation.

| Device structure | Size | Tested structure | Synaptic functions | Reference |
|---|---|---|---|---|
| Au/Pd/$WSe_2$ | 10 µm | Polymer electrolyte gated transistor | STP to LTP transformation | S1 |
| Pt/InGaZnO/Pt | Ø 0.5 mm | Vertical structure | STP, LTP, Learning experience | S2 |
| Au/SnSwe/BP/Au | 5 µm | BP−SnSe heterojunction | STDP, Potentiation, depression | S3 |
| $_{MoS2}$/hBN/SLG | ~ µm | Heterostructure, Floating gate engineering | pulsed potentiation and relaxation, STDP | S4 |
| IZO/P-doped $SiO_2$ | 80 µm | laterally coupled oxide-based protonic/electronic hybrid artificial synapse network | PPF, dynamic filtering and spatiotemporally correlated signal processing | S5 |
| Au/Ti/$MoS_2$ | ~ µm | Biopolymer electrolyte gated $MoS_2$ transistor | EPSC, STDP | S6 |
| Pt/Ag-doped $SiO_xN_y$/Pt | 10 µm | Inert electrodes sandwiched structure | STP, LTP | S7 |
| Ag/MgO/Pt | 2 µm | Electrochemical metallization | PPD, LTP, PPF | S8 |
| Au/Lix$MoS_2$/Au | 5 µm | Lateral structure | Synaptic competition and synaptic cooperation effects | S9 |
| TiN/$Ge_2Sb_2Te_5$/TiN | Ø 75 µm | T-cell phase transition area | Pair STDP | S10 |
| Pd/$Ta_2O_{5x}$/$TaO_y$/Pd | 1 µm | Crossbar structure | STDP, LTP | S11 |
| Ni/Nb-$SrTiO_3$/Ti | Ø 400 µm | MIM structure | learning, forgetting | S12 |
| Pt/InGaZnO/Pt | Ø 0.5 µm | Shadow mask patterned MIM | Learning experience | S13 |
| Pt/$TiO_2$/Pt | 2 µm | Vertical structure | Triplet-STDP, LTP | S14 |
| $HfO_x$/ta/$TaO_x$/Pt | 4 µm | MIM structure with sidewalls | Heterosynaptic interactions | S15 |
| Au/Ti/$MoS_2$ | 5 µm | multi-terminal memristors | Cooperation/competition | S16 |
| Pt/GO/Au | 50 $nm^2$ | CAFM tip-sample junction | Potentiation, PPF, EPSC relaxation, non-volatile RS | Our work |

**Table S2:** Cell size of cross-point and cross-bar devices fabricated by nanolithography.

| Device structure | Cell size | Fabrication technique | Reference |
|---|---|---|---|
| $Pt/TiO_2/Pt$ | 50 nm×50 nm | nanoimprint lithography | S17 |
| $TiN/Hf/HfO_x/TiN$ | 10 nm×10 nm | E-beam lithography | S18 |
| Pt/Cr/Ag-Si/Si/W | 100 nm×100 nm | E-beam lithography | S19 |
| Pt/GO/Au, Pt/GO/Cu | 50 $nm^2$ | - | Our work |

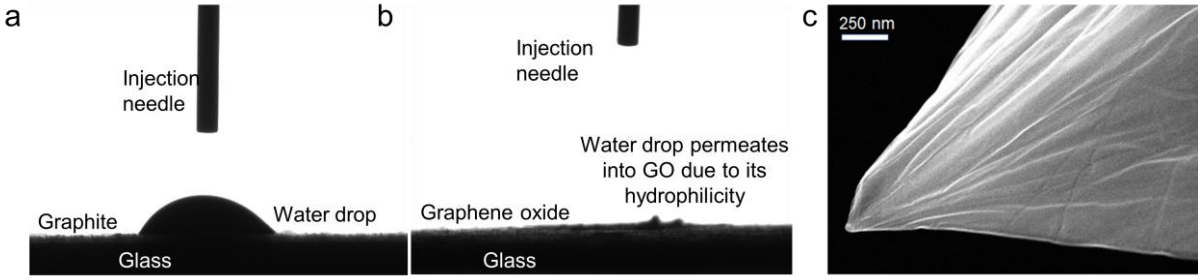


**Supplementary Figure 1:** (a) and (b) Wettability measurement of graphite and GO, respectively. GO exhibits good hydrophilic properties, indicating the existence of a large amount of oxygen-containing functional groups. (c) SEM image of CAFM tip (Type: Arrow CONTPt) after spray-coating with a ~100 nm thick GO film. The image shows conformal coating. GO is recognized by the formation of wrinkles.

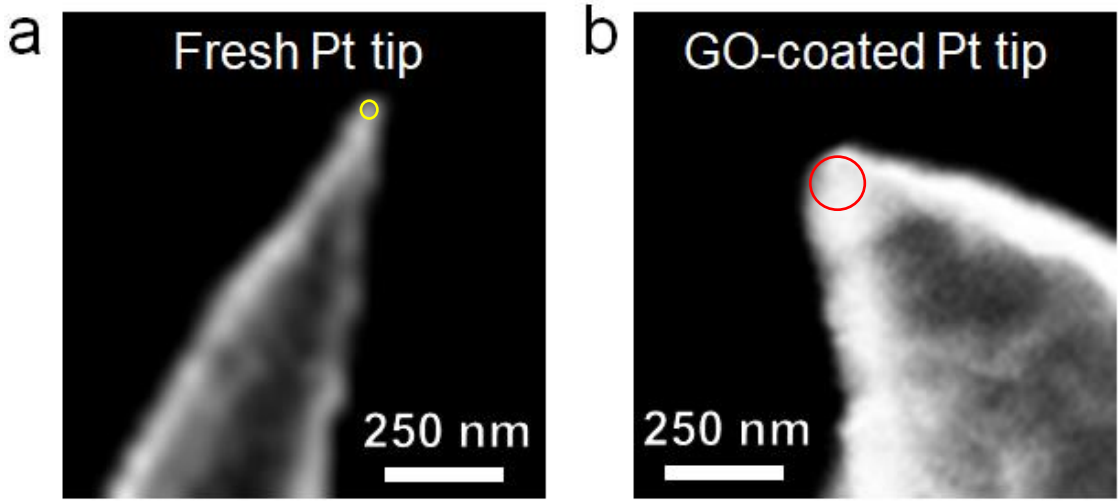


**Supplementary Figure 2:** Zoomed-in images of (a) fresh Pt tip (b) GO-coated Pt tip cropped from the SEM images in Figures 1c, d of the main text, respectively. The radius of each tip (highlighted with a yellow and red circles) can be estimated to be ~8 nm (fresh tip) and ~65 nm (GO-coated).

**Supplementary Note 1: Effective contact area between tip and sample**

According to Hertz's contact theory [S20-S21], the most used to study interactions between tip and sample in AFM systems [S20-S23], $A_C$ can be quantified as [S20-S21]:

$$A_c = \pi \cdot {r_c}^2 = \pi \left(\frac{F_c R_{tip}}{K}\right)^{2/3} \quad \text{with } \frac{1}{K} = \frac{3}{4}\left(\frac{1-v_1^2}{E_1} + \frac{1-v_2^2}{E_2}\right) \qquad \text{(Eq.S1)}$$

where $r_c$ is the contact radius (the radius of the contact area), $F_c$ is the contact force between tip and sample, $R_{tip}$ is the tip radius, $E_{1/2}$ are the elasticity moduli and $v_{1/2}$ are the Poisson ratios of tip and sample. $F_c$ is given by Hooke's law [S24]:

$$F_c = -k_c \cdot \delta_c + F_{ext} \qquad \text{(Eq. S2)}$$

where $k_c$ is the spring constant of the tip, $\delta_c$ is the tip deflection, and $F_{ext}$ is the sum of external forces, such as capillary forces, electrostatic forces and others [S25].

Ref.S26 reported calculations of $A_C$ for different $R_{tip}$, $F_C$, and tip/sample materials composition, giving a 1-1000 nm$^2$ range [S26]. However, the effective area ($A_{eff}$), defined as the sum of all the spatial locations on the surface of the sample electrically connected to the CAFM, across which the electrons can flow, also depends on relative humidity [S26], and the thickness of the water layer on the surface of tip and sample [S27]. Therefore, when studying insulating materials with a CAFM tip in air, $A_{eff}$ is normally>$A_C$ [S26]. We estimate the tip/sample contact area, i.e. the size of the Pt/GO/Au nano-synapses (formed by placing a Pt tip on GO/Au sample) and Pt/GO/Cu nano-synapses (formed by placing a Pt/GO tip on a Cu surface) to be very small (<50 nm$^2$) [S27].

Ref.S27 reported that the most (statistically) accepted value for $A_{eff}$ when using sharp Pt tips ($R_{tip}$ <25 nm) on the surface of $SiO_2$ is ~50 nm$^2$. This tip/sample system is similar to our Pt/GO/Au nano-synapses, with the only difference that our Pt tip is sharper ($R_{tip}$ ~8 nm, see Supplementary Fig.2a) and that the GO film is softer than Pt. According to Eq.1, a smaller $R_{tip}$ decreases $A_{eff}$, and softer materials increase $A_{eff}$. For this reason, in our experiments we use a very low deflection setpoint (i.e. $F_C$) ~0.2 V, to minimize tip penetration into the GO film. There is no tip penetration into GO because topographic AFM maps collected after tip landing on the GO surface do not show any hole. Therefore, the size of our Pt/GO/Au nano-synapses is slightly <50 nm$^2$.

When GO-coated Pt tips are placed in contact with the Cu surface in order to form Pt/GO/Cu nano-synapses, the radius of the GO-coated Pt tip is ~65 nm, Fig. S2b. Refs. S27-S28 reported that an increase of $R_{tip}$ by~20 times produces one order of magnitude increase of $A_C$ (from Eq. S1 this would be $20^{2/3}$ = 7.36). Therefore, as the radius of the GO-coated Pt tip is ~65 nm (i.e. ~8 times larger than that the~8nm size of the of Pt tip), the size of the Pt/GO/Cu nano-synapse (i.e. the tip/sample contact area) is not >500 nm$^2$.

*(see next page)*

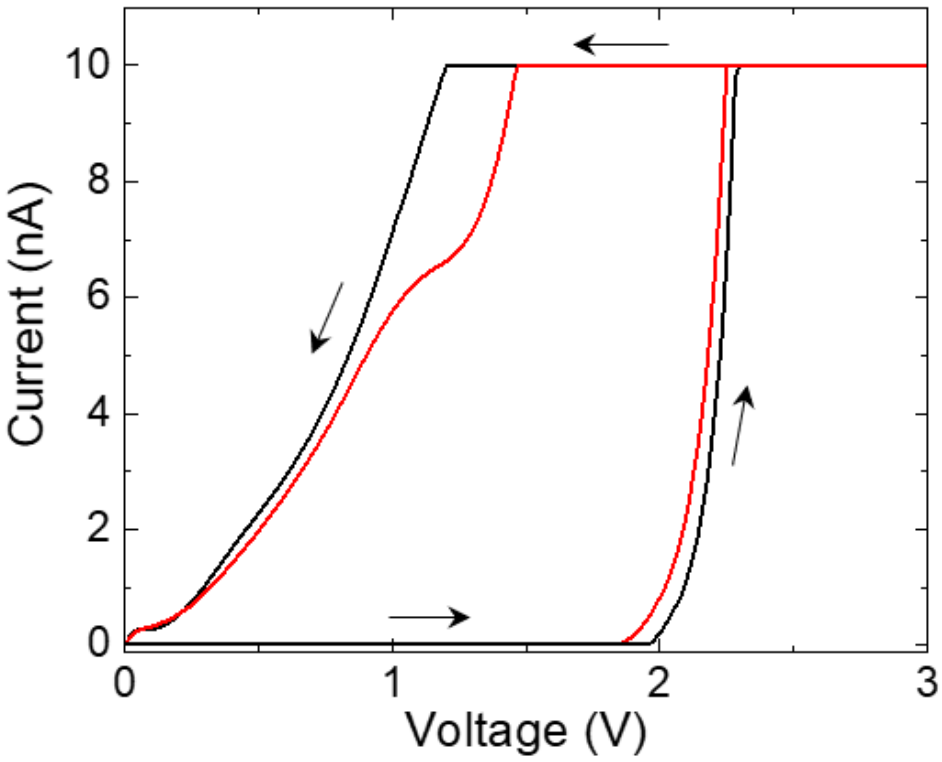


**Supplementary Figure 3:** *I-V* curves showing volatile resistive switching characteristics in Pt/GO/Au synapses. Each *I-V* curve (red and black) corresponds to different positions.

**Table S3:** Write current of memristive synapses with different device sizes.

| Synapse structure | Device size ($\mu m^2$) | Write voltage (V) | Write current / power 1st pulse | Write current/ power last pulse | # pulses | Ref. |
|---|---|---|---|---|---|---|
| Au/hBN/Au | 25 | 5.8 | 70 µA / 406 µW | 760 µA / 4.4 mW | 26 | S29 |
| Ag/CH3NH3PbI3-xClx/FTO | 5000 | 0.5 | 0.5 µA / 0.25 µW | 0.75 µA / 0.38 µW | 10 | S30 |
| Pt/$SiO_xN_y$:Ag/Pt | 100 | 2.8 | 250 µA / 700 µW | 1400 µA / 3.9 mW | 500 | S7 |
| TiN/$TaO_x$/Pt | 4 | 1 | 800 µA / 800 µW | 2200 µA / 2.2 mW | 300 | S31 |
| Ni/Nb-$SrTiO_3$/Ti | 160000 | 6 | 0.5 µA / 3 µW | 6 µA / 36 µW | 62 | S12 |
| Au/Ti/h-BN/Cu | 25 | 0.7 | 1 µA / 0.7 µW | 70 µA / 49 µW | 19 | S32 |
| Ag/$Zr_{0.5}Hf_{0.5}O_2$:GOQDs/Ag | 10000 | 0.8 | 200 µA / 160 µW | 3000 µA / 2.4 mW | 30 | S33 |
| Ag/N-GOQDs/Pt | 7850 | 0.3 | 100 µA / 30 µW | 2000 µA / 600 µW | 30 | S34 |
| Cu/p$V_3D_3$/AI | 25 | 2 ~4 | 750 µA / 2.3 mW | 3000 µA / 9 mW | 50 | S35 |
| Au/$WS_2$/PZT/Au | 24.3 | 3.5 | 0 µA / 0 µW | 0.15 µA / 0.53 µW | 10 | S36 |
| Ag/CιC:Ag/ITO | 10000 | 0.8~1.1 | 10 µA / 10 µW | 60 µA / 60 µW | 100 | S37 |
| ITO/ZnO/ITO | 22500 | 1 | 50 µA / 50 µW | 250 µA / 250 µW | 150 | S38 |
| W/Ag/MgO/Ag/W | 25 | 3 | 1300 µA / 4 mW | 2000 µA / 6 mW | 10 | S39 |
| Pt/LSO/TiN/Ti/$SiO_2$/Si | 0.64 | 0.1 | 30 µA / 0.3 µW | 300 µA / 30 µW | 100 | S40 |
| TiN/$HfO_2$/Ti/TiN | 1600 | 0.7 | 460 µA / 322 µW | 700 µA / 490 µW | 300 | S41 |
| Pt/WOx/Ti | 282600 | 2 | 3.6 µA / 7.2 µW | 5.2 µA / 10.4 µW | 50 | S42 |
| TiN /$HfO_2$/Pt | 1600 | 1 | 400 µA / 400 µW | 1000 µA / 1 mW | 300 | S43 |
| Pt/HfOx/ZnOx/TiN | 17662 | 2 | 420 µA / 840 µW | 540 µA / 1 mW | 80 | S44 |
| ITO/LiF/CuPc/Al | 10000 | 11 | 120 µA / 1.3 mW | 270 µA / 3 mW | 10 | S45 |
| Au/$C_3$N/PVPy/ITO | 250000 | 5 | 750 µA / 3.8 mW | 1800 µA / 9 mW | 14 | S46 |
| Pt/GO/Au | $5\times10^{-5}$ | 3 | 0.03 µA / 0.1 µW | 5 µA / 15 µW | 50 | This work |

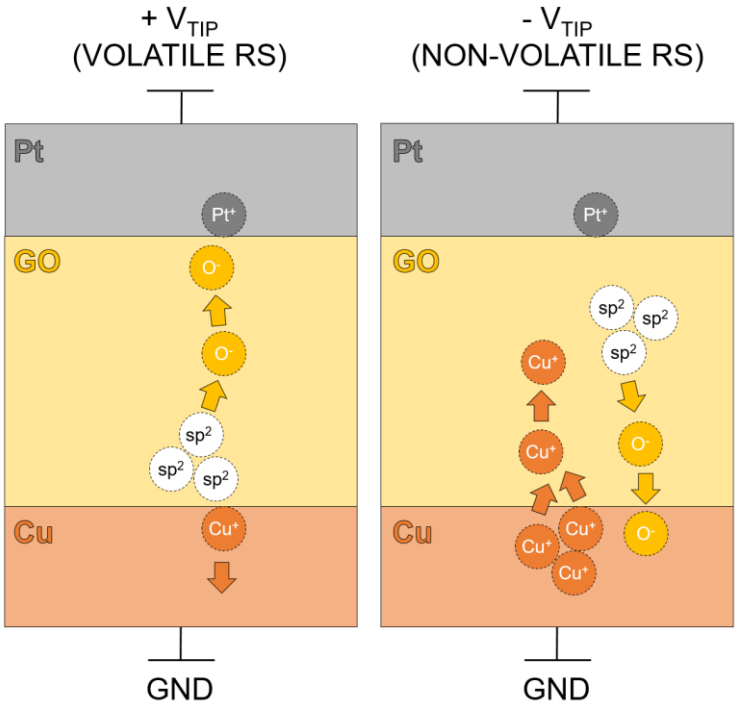


**Supplementary Figure 4:** Schematic switching mechanism in volatile regime (left) and non-volatile regime (right). The migration of oxygen requires low energy and, at the low current levels (<1 μA) presented in that regime, these defects are volatile. The migration of $Cu^+$ (or $Au^+$) ions produces non-volatile conductance changes because they are heavier and cannot recover their initial state when the bias is switched off.

**Supplementary Note 2: Thermal simulations**

We simulate the current across the Pt/GO/Au nano-synapse in LRS before the reset event, using the model of Ref. [S51], and comparing the resulting values with experiments. We estimate the resistance of the Pt/GO/Au nano-synapse and solve the three-dimensional heat equation [Eq. S5]. The simulation is designed taking into consideration that the thickness of the GO film is ~50 nm. The top Pt electrode has the shape of a CAFM tip, and the bottom electrode consists of a Au layer.

Eq.S5 is solved using a fully explicit finite difference method [S50]. Therefore, the features of the nano-synapses that are thermally dependent are correctly described. The grid consists of 301 × 301 × 751 nodes, with a uniform mesh with 0.2 nm grid mesh distance (in line with comparable simulations [S51-S52]). Dirichlet boundary conditions [S53] are employed at the outer electrode layer surfaces, and room temperature is assumed outside the device (due to the high electrode thermal conductivity (Au: 317 W/mK, Pt: 71.6 W/mK) [S54]). Perfectly matched layers (PML) are used at the lateral faces [S51, S55-S56] to describe open boundary problems, such as ours.

$$\dot{q} = -\nabla[k_{th}(x,y,z)\nabla T(x,y,z)] \quad \text{(Eq. S5)}$$

We account for Joule heating to determine the heat generation rate ($\dot{q}$) in Eq.S5. As the current is generated by applying a negative bias to the CAFM tip, it is expected to consist of $Au^+$ ions that migrate from the Au bottom electrode towards the cathode (Pt tip). A non-fully formed conductive path is assumed with high electrical conductance and truncated-cone shaped [S57-S58]. The temperature peak is achieved at the narrower part of this region, see Figure S5. The heat generation rate ($\dot{q}$) is calculated using the electrical conductivity and the electric field distribution in the Pt/GO/Au nano-synapse.

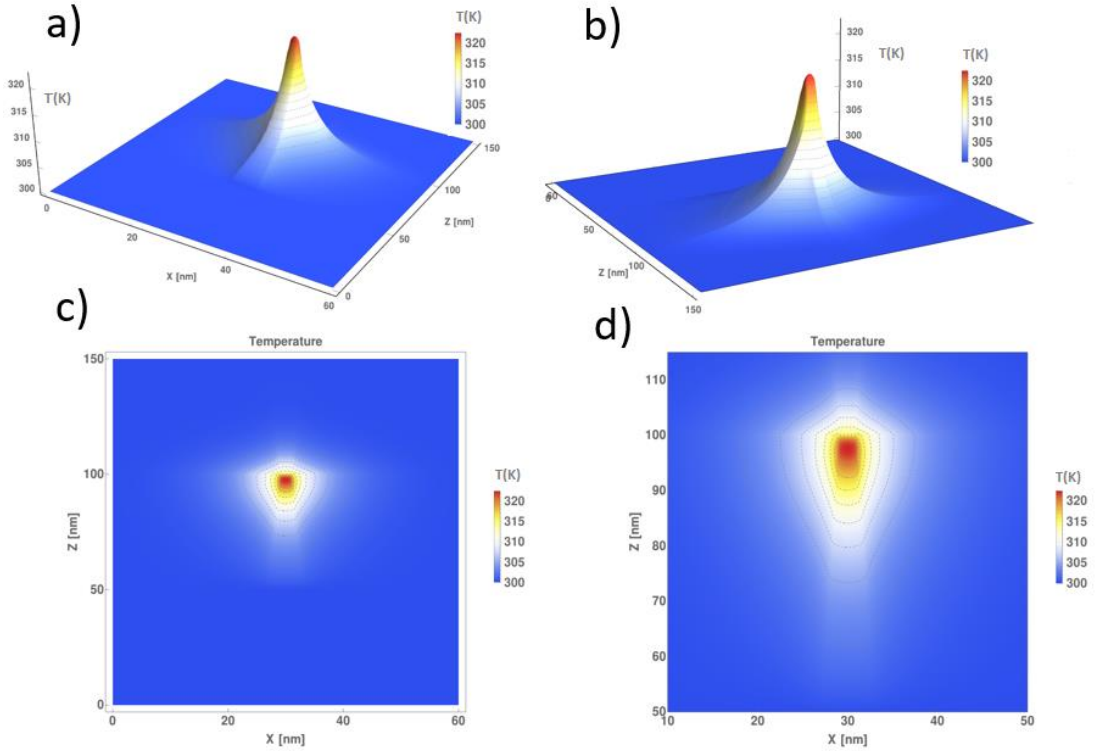


**Figure S5**: Three-dimensional temperature distribution for different cross-sections in the device structure (Fig. 1 in the main text). The simulations are performed for 6V in the LRS, the simulated current is equal to the experimental one for one of the cycles in Fig. 4c in the main text (30 µA). (a) Longitudinal cross-section in the XZ plane (the non-continuous conductive path extends from Z=50 to 100nm), taken in the middle of the simulation domain. The variations in the temperature distribution correspond to the limited extension of the AFM tip, affecting the final result. (b) Same cross-section as (a) from another bird's eye view. (c,d) contour plots of the temperature distributions in (a,b), respectively.

For the electrodes, the following thermal conductivity values are employed $K_{TH}$ (Au) = 317 W/Km [S54], $K_{TH}$ (Pt) =71.6 W/Km [S54]. The partially formed conductive path is assumed to have $K_{TH}$ (path)~15 W/Km consistent with that of Refs. [S52, S59]. For GO we use $K_{TH}$ (GO)~2.83 W/Km [S60]. The weighted residual method is employed to numerically solve the heat equation [S51, S61].

**Table S4:** Physical parameters used in the simulations [S51,S52,S54,S59,S60,S61]

| | | |
|---|---|---|
| $K_{TH}$ (Au) | 317 W $K^{-1}$ $m^{-1}$ | Cu thermal conductivity |
| $K_{TH}$ (path) | 15 W $K^{-1}$ $m^{-1}$ | Conductive path thermal conductivity |
| $K_{TH}$ (Pt) | 71.6 W $K^{-1}$ $m^{-1}$ | Pt thermal conductivity |
| $K_{TH}$ (GO) | 2.83 W $K^{-1}$ $m^{-1}$ | GO thermal conductivity |
| $\sigma_{CF\_path}$ | 1.67 x $10^6$ $\Omega^{-1}$ $m^{-1}$ | Conductive path conductivity |
| $T_0$ | 300 K | Room temperature |

A simulation is performed, using current and voltage data corresponding to the *I-V* curves measured in Fig. 4c in the main text, with the parameters in Table S5. The thermally activated physical mechanisms behind RS trigger the broadening of the gaps in the conductive path that gives the reset process (see Fig.4c in the main text). Therefore, the thermal description is crucial for the study of our Pt/GO/Au nano-synapses [S56-S57].

## References


[S1] Zhu, J. *et al*. Ion gated synaptic transistors based on 2D van der Waals crystals with tunable diffusive dynamics *Adv*. *Mater*. **30**, 1800195 (2018).

[S2] Wang, Z. Q. *et al*. Synaptic Learning and Memory Functions Achieved Using Oxygen Ion Migration/Diffusion in an Amorphous InGaZnO Memristor. *Adv*. *Funct*. *Mater*. **22**, 2759 (2012).

[S3] Tian, H. *et al*. Emulating Bilingual Synaptic Response Using a Junction-Based Artificial Synaptic Device. *ACS Nano* **11**, 7156 (2017).

[S4] Paul, T., Ahmed, T., Kanhaiya Tiwari, K., Singh Thakur, C., Ghosh, A. A high-performance MoS2 synaptic device with floating gate engineering for neuromorphic computing. *2D Mater.* **6**, 045008 (2019).

[S5] Zhu, L. Q., Wan, C. J., Guo, L. Q., Shi, Y., Wan, Q. Artificial synapse network on inorganic proton conductor for neuromorphic systems. *Nat. Commun.* **5**, 3158 (2014).

[S6] Jiang, J. *et al.* 2D electric-double-layer phototransistor for photoelectronic and spatiotemporal hybrid neuromorphic integration. *Nanoscale* **11**, 1360 (2019).

[S7] Wang, Z. *et al.* Memristors with diffusive dynamics as synaptic emulators for neuromorphic computing. *Nat*. *Mater*. **16**, 101–108 (2017).

[S8] Zhang, Y., Zhong, S., Song, L., Ji, X., Zhao, R. Emulating dynamic synaptic plasticity over broad timescales with memristive device. *Appl*. *Phys*. *Lett*. **113**, 203102 (2018).

[S9] Zhu, X., Li, D., Liang, X., Lu, W. D. Ionic modulation and ionic coupling effects in MoS2 devices for neuromorphic computing. *Nat*. *Mater*. **18**, 141 (2019).

[S10] Kuzum, D., Jeyasingh, R. G. D., Lee, B., Wong, H.S.P. Nanoelectronic Programmable Synapses Based on Phase Change Materials for Brain-Inspired Computing. *Nano Lett.* **12**, 2179-2186 (2012).

[S11] Kim, S. *et al*. Experimental Demonstration of a Second-Order Memristor and Its Ability to Biorealistically Implement Synaptic Plasticity. *Nano Lett*. **15**, 2203−2211 (2015).

[S12] Yin, X. B. et al. Mimicking the brain functions of learning, forgetting and explicit/implicit memories with SrTiO3-based memristive devices. *Phys. Chem. Chem. Phys.*, **18**, 31796-31802 (2016).

[S13] Wang, Z. Q. et al. Synaptic Learning and Memory Functions Achieved Using Oxygen Ion Migration/Diffusion in an Amorphous InGaZnO Memristor. *Adv*. *Funct*. *Mater*. **22**, 2759–2765 (2012).

[S14] Wei, S. L. et al. Emulating long-term synaptic dynamics with memristive devices. arXiv:1509.01998.

[S15] Yang, Y. et al. Multifunctional nanoionic devices enabling simultaneous heterosynaptic plasticity and efficient in-memory boolean logic. *Adv*. *Electron*. *Mater*. **3**, 1700032 (2017).

[S16] Sangwan, V. K. et al. Multi-terminal memtransistors from polycrystalline monolayer molybdenum disulfide. *Nature* **554**, 500 (2018).

[S17] J. J. Yang, et al. Memristive switching mechanism for metal/oxide/metal nanodevices. *Nat. Nanotechnol*. **3**, 429 (2008).

[S18] B. Govoreanu et al. 10x10 $nm^2$ Hf/$HfO_x$ crossbar resistive RAM with excellent performance, reliability and low-energy operation. *IEEE IEDM* DOI: 10.1109/IEDM.2011.6131652 (2011).

[S19] S. H. Jo, et al. Nanoscale memristor device as synapse in neuromorphic systems. *Nano Lett.* **10**, 1297-1301 (2010).

[S20] Olbrich, A. "Characterisation of thin dielectrics by means of modified atomic force microscopy", PhD thesis, University of Regensburg, Regensburg, Germany (1999).

[S21] B. Bhushan (Ed.), Springer Handbook of Nanotechnology, Springer-Verlag, Berlin (2004).

[S22] Ruskell, T. G. *et al.* Novel millimeter-wave near-field resistivity microscope. *Appl*. *Phys. Lett*. **68**, 9 (1996).

[S23] A. Born, "Applications of scanning capacitance microscopy and scanning probe microscopy techniques in nanotechnology", PhD thesis, University of Hamburg, Germany, http://www.physnet.unihamburg.de/services/fachinfo/_Volltexte/Axel_Born/Axel_Bron.htm (accessed on January 18, 2015).

[S24] Louey, M. D.; Mulvaney, P.; Stewart, P. J. *J. Pharm. Biomed. Anal.* **29**, 559 (2001).

[S25] Cappella, B.; Dietler, G. Force-distance curves by atomic force microscopy. *Surf. Sci. Rep.* **34**, 1 (1999).

[S26] Pan, C., Shi., Y., Hui, F., Grustan-Gutierrez, E. & Lanza, M. in Conductive Atomic Force Microscopy: Application in Nanomaterials (ed. Lanza, M.) Ch. 1 (Wiley-VCH, 2017).

[S27] Frammeblsberger, W., Benstetter, G., Kiely, J., Stamp, R. C-AFM-based thickness determination of thin and ultra-thin SiO2 films by use of different conductive-coated probe tips. *Appl. Surf. Sci.* **253**, 3615-3626 (2007).

[S28] Frammelsberger, W., Benstetter, G., Kiely, J., Stamp, R. Thickness determination of thin and ultra-thin SiO2 films by C-AFM IV-spectroscopy. *Appl. Surf. Sci.* **252**, 2375 (2006).

[S29] Chen, S. C. *et al.* Wafer-scale integration of 2D materials in high-density memristive crossbar arrays for artificial neural networks. *Nat. Electron.* 3, 638-645 (2020).

[S30] Yoo, E. *et al.* Bifunctional resistive switching behavior in an organolead halide perovskite based Ag/$CH_3NH_3PbI_{3-x}Cl_x$/FTO structure. *J. Mater. Chem. C* 7824-7830 (2016).

[S31] Wang, Z. W. *et al.* Engineering incremental resistive switching in TaOx based memristors for brain-inspired computing. *Nanoscale* **8**, 14015-14022 (2016).

[S32] Xiao, M. One-dimensional Titanium Dioxide Nanomaterial based Memristive Device and its Neuromorphic Computing Applications, PhD thesis, *UWSpace*. http://hdl.handle.net/10012/14872 (2019).

[S33] Yan, X. B. *et al.* Graphene Oxide Quantum Dots Based Memristors with Progressive Conduction Tuning for Artificial Synaptic Learning. *Adv. Funct. Mater.* 1803728 (2018).

[S34] Sokolov, A.S. *et al.* Silver-Adapted Diffusive Memristor Based on Organic Nitrogen-Doped Graphene Oxide Quantum Dots (N-GOQDs) for Artificial Biosynapse Applications. *Adv. Funct. Mater.* **29**, 1807504 (2019).

[S35] Jiang, B. C. *et al.* Polymer analog memristive synapse with atomic-scale conductive filament for flexible neuromorphic computing system *Nano Lett.* **19**, 839−849 (2019).

[S36] Luo, Z-. D. *et al.* Artificial Optoelectronic Synapses Based on Ferroelectric Field-Effect Enabled 2D Transition Metal Dichalcogenide Memristive Transistors. *ACS Nano* **14**, 746–754 (2020).

[S37] Ge, J. *et al.* Memristive synapses with high reproducibility for flexible neuromorphic networks based on biological nanocomposites. *Nanoscale*, **12**, 720-730 (2020).

[S38] Chandrasekaran, S., Simanjuntak, F. M., Panda, D., Tseng, T.-Y. Enhanced Synaptic Linearity in ZnO-Based Invisible Memristive Synapse by Introducing Double Pulsing Scheme. *IEEE Transactions on Electron Devices* **66**, 4722-4726 (2019).

[S39] Sun, J. *et al.* Physically Transient Memristive Synapse With Short-Term Plasticity Based on Magnesium Oxide. *IEEE Electron Device Letters* **40**, 706-709 (2019).

[S40] Chen, J. *et al.* LiSiOX-Based Analog Memristive Synapse for Neuromorphic Computing. IEEE Electron Device Letters **40**, 542-545 (2019).

[S41] Covi, E. *et al.* Analog Memristive Synapse in Spiking Networks Implementing Unsupervised Learning. *Front. Neurosci.* **10**, 482 (2016).

[S42] Lin, Y. *et al.* Transferable and Flexible Artificial Memristive Synapse Based on WOx Schottky Junction on Arbitrary Substrates. *Adv. Funct. Mater.* **4**, 1800373 (2018).

[S43] Covi. E. *et al.* Spike-driven threshold-based learning with memristive synapses and neuromorphic silicon neurons. *J. Phys. D: Appl. Phys.* **51** 344003 (2018).

[S44] Wang, L. G. *et al.* Synaptic Plasticity and Learning Behaviors Mimicked in Single Inorganic Synapses of Pt/HfOx/ZnOx/TiN Memristive System. *Nanoscale Research Letters* **12**, 65 (2017).

[S45] Wang, L. *et al.* Rectification-Regulated Memristive Characteristics in Electron-Type CuPc-Based Element for Electrical Synapse. *Adv. Electron. Mater.* 3, 1700063 (2017).

[S46] Zhou, L. *et al.* Tunable synaptic behavior realized in $C_3N$ composite based memristor. *Nano Energy* **58**, 293-303 (2019).
[S47] Pan, C. *et al*. Model for multi-filamentary conduction in graphene/hexagonal-boron-nitride/graphene based resistive switching devices. *2D Mater.* **4**, 025099 (2017).
[S48] Roldán, J. B. *et al.* Multivariate analysis and extraction of parameters in resistive RAMs using the Quantum Point Contact model. *J. Appl. Phys.* **123**, 014501 (2018).
[S49] Lee, D. *et al.* Quantum confinement-induced tunable exciton states in graphene oxide. *Sci. Rep.* **3**, 2250 (2013).
[S50] Mazumder, S. Numerical methods for partial differential equations : finite difference and finite volume methods, Academic Press, 2015.
[S51] Maestro, M. *et al*. Unipolar resistive switching behavior in $Al_2O_3/HfO_2$ multilayer dielectric stacks: fabrication, characterization and simulation. *Nanotechnology* **31**, 135202 (2020).
[S52] Aldana, S. et al. A 3D kinetic Monte Carlo simulation study of resistive switching processes in Ni/HfO2/Si-n+-based RRAMs. J. Phys. D: Appl. Phys. 50, (2017).
[S53] Cheng, A., D., Cheng T. Heritage and early history of the boundary element method, *Engineering Analysis with Boundary Elements*, **29**, 268–302 (2005).
[S54] https://www.engineeringtoolbox.com/thermal-conductivity-metals-d_858.html
[S55] Lantos, N., Nataf, F. Perfectly matched layers for the heat and advection–diffusion equations, *J. Comput. Phys.* **229**, 9042–9052 (2010).
[S56] Moreno, E. *et al*. Implementation of Open Boundary Problems in Photo-Conductive Antennas by Using Convolutional Perfectly Matched Layers. *IEEE Trans. Antennas Propag.* **64**, 4919–4922 (2016).
[S57] Aldana, S. *et al*. An in-depth description of bipolar resistive switching in Cu/HfOx/Pt devices, a 3D Kinetic Monte Carlo simulation approach. *J. Appl. Phys.* **123**, 154501 (2018).
[S58] Rodriguez, N. *et al*. Resistive switching and charge transport in laser-fabricated graphene oxide memristors: a Time Series and Quantum Point Contact modelling approach. *Materials* **12**, 3734 (2019).
[S59] Ielmini, D. Modeling the universal set/reset characteristics of bipolar RRAM by field- and temperature-driven filament growth. *IEEE Trans. Electron Devices.* **58**, 4309-4317 (2011).
[S60] Zeng W. *et al.* Defect-engineered reduced graphene oxide sheets with high electric conductivity and controlled thermal conductivity for soft and flexible wearable thermoelectric generators. *Nano Energy* **54**, 163-174 (2018).
[S61] B.A. Finlayson, The method of weighted residuals and variational principles: with application in fluid mechanics, heat and mass transfer, Academic Press, (1972).